


Particle-resolved multiphase Rayleigh-Bénard convectionXianyang Chen ^{*}*Department of Mechanical Engineering, University of Houston, Houston, Texas 77204-4006, USA*Andrea Prosperetti [†]*Department of Mechanical Engineering, University of Houston, Houston, Texas 77204-4006, USA;
Faculty of Science and Technology, University of Twente, 7500 AE Enschede, The Netherlands;
and Department of Mechanical Engineering, Johns Hopkins University, Baltimore, Maryland 21218, USA*

(Received 9 February 2024; accepted 8 April 2024; published 10 May 2024)

Numerical simulations of Rayleigh-Bénard convection with suspended particles are described. The Rayleigh number is 10^7 and the Prandtl number unity. The particles have a finite size and are individually resolved by the PHYSALIS method which combines a regular Cartesian grid with a local spectral method around each particle. Two cells are considered, a cubic one with up to 3000 particles and a quasi-two-dimensional one with aspect ratio 2 with up to 1000 particles. In both cases the maximum volume fraction is about 20%. Emphasis is placed on the key role played by particle “dunes” in the resuspension of particles after they have fallen to the ground. Dunes are structures formed on the bottom of the cell by the nearly horizontal fluid velocity field which pushes particles from the foot of the descending plume to that of the ascending one. Without this mechanism which, by its very nature, cannot be captured by point-particle models, very few particles, if any, would be resuspended. Bigger dunes, formed by more or heavier particles, are more effective than smaller ones in causing particle resuspension provided the total number and mass of particles is not too large. A small number of particles produces a modest improvement on the Nusselt number, but the effectiveness of particles as heat carriers is soon overshadowed by the weight they add to the mixture which slows down the circulation. The efficiency with which particles extract gravitational energy from the fluid reaches 20%, far higher than previous estimates in the literature which place it below 1%.

DOI: [10.1103/PhysRevFluids.9.054301](https://doi.org/10.1103/PhysRevFluids.9.054301)**I. INTRODUCTION**

Rayleigh-Bénard convection—the gravity-driven naturally occurring flow between two horizontal plates, the lower one hotter than the upper one—is one of the standard problems in fluid mechanics with a history that goes back over a century and a very voluminous literature. Much less copious is the literature on the two-phase version of the problem, in which solid particles are suspended in the fluid. Flows of this type occur in the transport of particles by oceanic or atmospheric currents (see, e.g., Refs. [1,2]), in magma chambers (see, e.g., Ref. [3]), and in the air circulation in rooms and other built spaces (see, e.g., Refs. [4–6]), to name a few examples.

Most of the existing studies are based on Lagrangian-Eulerian point-particle models which, by their very nature, can simulate particle settling but not their resuspension. For this reason authors have been forced to study either the transient version of the problem (see, e.g., Ref. [7]) or to

^{*}xchen88@central.uh.edu[†]aprosp@central.uh.edu

maintain a statistically steady situation by artificially reinjecting the particles once they reached the bottom plate. The authors of Refs. [8,9] did so by reinjecting the particles at the top plate, while those of Ref. [10] reinjected them in the bottom 10% of the cell. Neither procedure is very satisfactory as they artificially add energy to the system preventing the study of the pure effect of particles on the fluid circulation. The procedure of Ref. [10] minimizes this artifact but reliance on the fluid convection to resuspend particles reinjected near the bottom plate has the consequence that only very light particles, with a terminal velocity about 1% of the convection free-fall velocity [see Eq. (2.6) below for a definition] could remain in suspension, while heavier ones kept circulating near the bottom of the cell. Other authors, who studied the so-called vertical natural convection, in which the circulation is established between two vertical plates maintained at different temperatures, faced the same problem and handled it in similar ways, allowing the particles to settle (see, e.g., Ref. [11]) or artificially reinjecting them (see, e.g., Ref. [12]).

It appears that the only way in which the difficulties encountered in these studies can be satisfactorily addressed is by simulations which account for the finite size of the particles. Not many studies of this type can be found in the literature. Notable examples are papers by Kajishima and his group [13–15], who considered neutrally buoyant particles with such a high thermal conductivity that heat transfer on particle collision was an important process.

In the present paper we describe particle-resolved simulations in which the particle-fluid exchange of momentum and heat is accounted for by the combination of a uniform finite-difference grid and a spectral method in the neighborhood of each particle (see Sec. IV for a brief description). We consider a Rayleigh number of 10^7 , a unity Prandtl number and two cells, one cubic and one quasi-two-dimensional with aspect ratio 2 (according to the long horizontal dimension). The particle numbers are up to 3000 in the cubic cell and up to 1000 in the other one; in both cases, the maximum volume fraction is close to 20%. This volume fraction is large enough that, in the cubic cell, the results show the beginning of a transition toward a porous-medium behavior.

A major focus of the paper is the role played by bottom “dunes” in the resuspension of particles fallen to the ground. This mechanism was first identified experimentally in Ref. [16] but it does not seem to have been considered further in the literature. The efficient particle resuspension rendered possible by dunes greatly increases the conversion efficiency of gravitational energy from fluid to particles. We find an efficiency of about 20%, far exceeding the estimates of less than 1% given in Ref. [17].

II. MATHEMATICAL FORMULATION

The fluid satisfies the standard Boussinesq model (see, e.g., Ref. [18]) with a temperature-dependent density given by

$$\rho(T) = \rho_0[1 - \beta(T - T_0)], \quad (2.1)$$

in which $T_0 = \frac{1}{2}(T_h + T_c)$ is the reference temperature and ρ_0 the fluid density at $T = T_0$; β is the (constant) thermal expansion coefficient, and T_h and $T_c < T_h$ the fixed temperatures of the bottom and top no-slip boundaries, respectively. The continuity, momentum, and energy equations are given by

$$\nabla \cdot \mathbf{u} = 0, \quad (2.2)$$

$$\partial_t \mathbf{u} + \mathbf{u} \cdot \nabla \mathbf{u} = -\frac{1}{\rho_0} \nabla p + \nu_f \nabla^2 \mathbf{u} + [1 - \beta(T - T_0)] \mathbf{g}, \quad (2.3)$$

$$\partial_t T + \mathbf{u} \cdot \nabla T = D_f \nabla^2 T. \quad (2.4)$$

Here \mathbf{u} , p , and T are the velocity, pressure, and temperature fields; \mathbf{g} is the acceleration of gravity; and ν_f and D_f are the (constant) kinematic viscosity and thermal diffusivity, respectively. Nondimensionalization of (2.2), (2.3), and (2.4) leads to the well-known dimensionless Rayleigh

and Prandtl numbers, Ra and Pr, defined by

$$\text{Ra} = \frac{\beta(T_h - T_c)gH^3}{\nu_f D_f} \quad \text{and} \quad \text{Pr} = \frac{\nu_f}{D_f}, \quad (2.5)$$

with $g = \|\mathbf{g}\|$. A characteristic velocity of the problem is the free-fall velocity U_f defined by

$$U_f = \sqrt{g\beta(T_h - T_c)H}. \quad (2.6)$$

The particles translate with velocity \mathbf{U}_p according to Newton's law,

$$m_p \frac{d\mathbf{U}_p}{dt} = m_p \mathbf{g} + \mathbf{f}_{\text{tot}}^{\text{hd}} + \mathbf{f}^{\text{coll}}, \quad (2.7)$$

in which $m_p = \rho_p v_p = \frac{\pi}{6} d_p^3 \rho_p$, with ρ_p the (constant) particle density and v_p the particle volume, is the particle mass, equal for all the particles, and \mathbf{f}^{coll} is the collision force with other particles or with the boundaries of the domain (see Ref. [19]). The total hydrodynamic force $\mathbf{f}_{\text{tot}}^{\text{hd}}$ is given by

$$\mathbf{f}_{\text{tot}}^{\text{hd}} = \oint_{s_p} \boldsymbol{\sigma} \cdot \mathbf{n}_p ds_p, \quad (2.8)$$

with the integration of the fluid stress $\boldsymbol{\sigma}$ over the particle surface s_p ; \mathbf{n}_p is the unit normal directed out of the particle. This expression accounts for the effects of the entire fluid stress on the particle, including flow effects and buoyancy, but it is useful to explicitly identify the latter by writing identically

$$\mathbf{f}_{\text{tot}}^{\text{hd}} = \oint_{s_p} [\boldsymbol{\sigma} \cdot \mathbf{n}_p + \rho(T_p)(\mathbf{g} \cdot \mathbf{x})\mathbf{n}_p] ds_p - \oint_{s_p} \rho(T_p)(\mathbf{g} \cdot \mathbf{x})\mathbf{n}_p ds_p, \quad (2.9)$$

in which \mathbf{x} is the position vector of the integration point. The second integral can be evaluated explicitly with the result $\rho(T_p)v_p\mathbf{g}$. With the definition

$$\mathbf{f}^{\text{hd}} = \oint_{s_p} [\boldsymbol{\sigma} \cdot \mathbf{n}_p + \rho(T_p)(\mathbf{g} \cdot \mathbf{x})\mathbf{n}_p] ds_p, \quad (2.10)$$

we can therefore rewrite (2.7) as

$$m_p \frac{d\mathbf{U}_p}{dt} = [\rho_p - \rho(T_p)]v_p\mathbf{g} + \mathbf{f}^{\text{hd}} + \mathbf{f}^{\text{coll}}, \quad (2.11)$$

which clearly separates the buoyancy force from the force \mathbf{f}^{hd} purely due to flow. The particle rotation is governed by

$$I_p \frac{d\boldsymbol{\Omega}_p}{dt} = \mathbf{I}^{\text{hd}} + \mathbf{I}^{\text{coll}}, \quad (2.12)$$

with $I_p = \frac{1}{10} m_p d_p^2$ the moment of inertia, $\boldsymbol{\Omega}_p$ the angular velocity of rotation, and \mathbf{I}^{coll} the couple due to collisions (see Ref. [19]). The hydrodynamic couple \mathbf{I}^{hd} is given by

$$\mathbf{I}^{\text{hd}} = \oint_{s_p} a \mathbf{n}_p \times (\boldsymbol{\sigma} \cdot \mathbf{n}_p) ds_p, \quad (2.13)$$

with $a = \frac{1}{2} d_p$ the particle radius. For the particle temperature we use the lumped-capacitance approximation according to which

$$c_{pp} m_p \frac{dT_p}{dt} = - \oint_{s_p} \mathbf{q} \cdot \mathbf{n}_p ds_p \equiv -Q, \quad (2.14)$$

with c_{pp} the constant-pressure specific heat, T_p the particle temperature, and $\mathbf{q} \cdot \mathbf{n}_p$ the net heat flux out of the particle at the particle surface. Conditions for the validity of this approximation will be addressed below after (2.17).

TABLE I. Some particle-density dependent parameter values used in the present simulations. The other parameters were held fixed: $\text{Ra} = 10^7$, $\text{Pr} = 1$, $T_h - T_c = 4$, and $\beta = 0.1$.

| ρ_p/ρ_0 | Re_p | Nu_p | St | St _{th} | St _{th} | U_{term}/U_f | $\rho_p/\rho(T_c)$ | $\rho_p/\rho(T_h)$ |
|-----------------|---------------|---------------|---------------------|---------------------|------------------|-----------------------|--------------------|--------------------|
| | | | $c_{pp}/c_{pf} = 1$ | $c_{pp}/c_{pf} = 5$ | | | | |
| 1.1 | 10.0 | 3.89 | 0.28 | 0.37 | 1.85 | 0.063 | 0.917 | 1.38 |
| 1.2 | 16.9 | 4.47 | 0.26 | 0.35 | 1.75 | 0.11 | 1.00 | 1.50 |
| 1.4 | 28.0 | 5.17 | 0.25 | 0.36 | 1.80 | 0.18 | 1.17 | 1.75 |

The particle mechanical relaxation time is obtained from a simplified version of the particle momentum equation with the same form as (2.11) except that $\mathbf{f}^{\text{coll}} = 0$ and $\mathbf{f}^{\text{hd}} = -3\pi d_p \rho_0 \nu_f f(\text{Re}_p) \mathbf{U}_p$ with $f(\text{Re}_p) = 1 + 0.15 \text{Re}_p^{0.687}$ the well-known correction to the Stokes law of the Schiller-Naumann correlation (see, e.g., Ref. [20]). By considering the vertical component of this equation and setting the left-hand side to zero we have an implicit equation from which the terminal velocity of individual particles can be determined

$$U_{\text{term}} = \frac{(\rho_p - \rho_0) g d_p^2}{18 \rho_0 \nu_f [1 + 0.15 \text{Re}_p^{0.687}]}. \quad (2.15)$$

After this step we can define the mechanical particle relaxation time as

$$\tau_p = \frac{m_p}{3\pi d_p \rho_0 \nu_f f(\text{Re}_p)}, \quad (2.16)$$

with Re_p calculated in correspondence of U_{term} as a representative particle-fluid relative velocity. The particle thermal relaxation time $\tau_{p,\text{th}}$ is defined by a similar procedure starting from a simplified form of the particle energy equation (2.14) in which the right-hand side is replaced by $\pi d_p^2 h_p (T - T_p)$ with the heat transfer coefficient $h_p = (k_f/d_p) \text{Nu}_p$ expressed in terms of the fluid thermal conductivity k_f and a particle Nusselt number $\text{Nu}_p = 2 + 0.6 \text{Pr}^{1/3} \text{Re}_p^{1/2}$ with Re_p again calculated in correspondence of the terminal velocity (see, e.g., Refs. [20–22]). The result is

$$\tau_{p,\text{th}} = \frac{d_p^2 \rho_p c_{pp}}{6 k_f \text{Nu}_p}. \quad (2.17)$$

The lumped-capacitance approximation is justified provided the diffusion length in the particle, of order $\sqrt{(k_p/\rho_p c_{pp}) \tau_{p,\text{th}}}$, with k_p the thermal conductivity of the particle material, is sufficiently greater than the particle radius $\frac{1}{2} d_p$, which requires $k_p/k_f > \frac{3}{2} \text{Nu}_p$. With $\text{Nu}_p \lesssim 5$ (see Table I) the limit on the magnitude of k_p/k_f is not so stringent as to make the particle-particle heat transfer on collision a significant process in the thermofluid dynamics of the system. The neglect of direct particle-particle heat transfer on contact is a good approximation because the area of the particle surface through which transfer takes place on contact is much smaller than that through which the particle-fluid heat transfer occurs. Since the present mathematical model solves the energy equation in the fluid accounting for conduction and convection, the heat transfer mediated by the interstitial fluid is dominant and is properly taken into account. This argument could be unsatisfactory if the particle thermal conductivity k_p was orders of magnitude greater than that of the fluid, as in Refs. [13–15] or if contacting particles could have very different temperatures. Validity of the lumped capacitance approximation does not require such extreme values of the ratio k_p/k_f and in weakly turbulent Rayleigh-Bénard convection in a fluid with $\text{Pr} \sim O(1)$, as considered here, large temperature gradients cannot develop. Particles that come into contact have been surrounded by the fluid throughout their motion and therefore, provided their thermal properties are not very different from those of the fluid, their temperatures cannot be very different either (and, in any case, maximum temperature differences are bounded by $T_h - T_c$). Direct particle-particle heat transfer would also

be hindered by the contact resistance. These considerations justify omission of this effect. The fluid timescale is estimated as $\tau_f = H/U_f$ from which the particle mechanical and thermal Stokes numbers, St and St_{th} , follow as

$$St = \frac{U_f \tau_p}{H}, \quad St_{th} = \frac{U_f \tau_{p,th}}{H}. \quad (2.18)$$

III. BALANCE RELATIONS

In the theory of single-phase Rayleigh-Bénard convection there are two exact relations that embody two different aspects of the principle of conservation of energy. The first one establishes the fact that, in a time-averaged sense, the gravitational potential energy acquired per unit time by the fluid is entirely dissipated by viscosity

$$E_f \equiv -\beta \rho_0 \mathbf{g} \cdot \int_V \overline{(T - T_0) \mathbf{u}} dV = \frac{1}{2\mu_f} \int_V \overline{\boldsymbol{\tau} : \boldsymbol{\tau}} dV, \quad (3.1)$$

where $\mu_f = \rho_0 \nu_f$ is the fluid viscosity parameter, $\boldsymbol{\tau}$ is the viscous stress tensor, the overline denotes the time average, and the integrals are extended to the entire cell volume. The second one states that, again in a time-average sense, the nondimensional thermal energy imparted to the cell base, i.e., the Nusselt number Nu , in part is conducted through the cell and in part is dissipated by viscosity,

$$Nu = 1 + \frac{1}{2\mu_f \rho_0 \beta g D_f (T_h - T_c) S} \int_V \overline{\boldsymbol{\tau} : \boldsymbol{\tau}} dV. \quad (3.2)$$

Here S is the common area of the cell base and top and

$$Nu = \frac{H}{k_f (T_h - T_c) S} \int_{S_t} \overline{q_{z,t}} dS_t = \frac{H}{k_f (T_h - T_c) S} \int_{S_b} \overline{q_{z,b}} dS_b, \quad (3.3)$$

with the subscripts t and b denoting the top and bottom plates. The equality between the time-averaged bottom and top Nusselt numbers is a consequence of the fluid energy equation (2.4) integrated over the volume. By (3.1), (3.2) can be cast into the alternative form,

$$Nu = 1 + \frac{1}{D_f (T_h - T_c) S} \int_V \overline{(T - T_0) u_z} dV = 1 + \frac{E_f}{\beta \rho_0 g D_f (T_h - T_c) S}. \quad (3.4)$$

These relations are modified by the presence of finite-size particles. The analog of (3.1) is obtained from the balance equation for the fluid kinetic energy $\frac{1}{2} \rho_0 \mathbf{u} \cdot \mathbf{u}$ after integrating over the fluid volume V_f and averaging over time,

$$-\beta \rho_0 \mathbf{g} \cdot \int_{V_f} \overline{(T - T_0) \mathbf{u}} dV_f = \frac{1}{2\mu_f} \int_{V_f} \overline{\boldsymbol{\tau} : \boldsymbol{\tau}} dV_f - \sum_{\alpha=1}^{N_p} \overline{(\mathbf{U}_\alpha \cdot \mathbf{f}_\alpha^{\text{coll}} + \boldsymbol{\Omega}_\alpha \cdot \mathbf{I}_\alpha^{\text{coll}})}, \quad (3.5)$$

with $\mathbf{f}_\alpha^{\text{coll}}$ and $\mathbf{I}_\alpha^{\text{coll}}$ the collisional contributions to the force and couple acting on the α particle.

To generalize the second relation (3.4) we calculate the time derivative of the fluid gravitational potential energy density $-\rho(T) \mathbf{g} \cdot \mathbf{x}$, integrate over the fluid volume V_f , and average over time to find

$$Nu = 1 + \frac{E_f + E_p}{\beta \rho_0 g D_f (T_h - T_c) S} + \frac{1}{k_f (T_h - T_c) S} \sum_{\alpha=1}^{N_p} \oint_{S_\alpha} \overline{z \mathbf{q} \cdot \mathbf{n}_\alpha} dS_\alpha, \quad (3.6)$$

in which \mathbf{n}_α is the unit normal on the surface of the α particle directed into the fluid and

$$E_p = -v_p \rho_p \mathbf{g} \cdot \sum_{\alpha=1}^{N_p} \overline{[\rho_p - \rho(T_p^\alpha)] \mathbf{U}_\alpha} = -v_p \rho_0 \beta g \cdot \sum_{\alpha=1}^{N_p} \overline{(T_p^\alpha - T_0) \mathbf{U}_\alpha} \quad (3.7)$$

is, similarly to E_f , the average gravitational potential energy of the particles and the last step follows from the fact $\mathbf{g} \cdot \sum_{\alpha} \overline{\mathbf{U}_{\alpha}} = 0$. The last term in (3.6) would vanish if the particles were to transfer an equal amount of heat to the fluid above and below the cell midplane $z = 0$. This point is addressed in connection with Fig. 8. The actual calculation of this term is facilitated by writing it identically as

$$\overline{\oint_{S_{\alpha}} z \mathbf{q} \cdot \mathbf{n}_{\alpha} ds_{\alpha}} = z_{\alpha} \overline{\oint_{S_{\alpha}} \mathbf{q} \cdot \mathbf{n}_{\alpha} ds_{\alpha}} + \overline{\oint_{S_{\alpha}} (z - z_{\alpha}) \mathbf{q} \cdot \mathbf{n}_{\alpha} ds_{\alpha}}, \quad (3.8)$$

with z_{α} the vertical coordinate of the center of the α th particle. Explicit expressions for the two integrals in this relation are given in (4.3) and (4.4) below.

The analog of another well-known single-phase relation can also be proven in a similar way. We multiply the fluid energy equation by T , integrate over the fluid volume, and take the time average to find

$$\text{Nu} = \frac{H}{(T_h - T_c)^2 S} \overline{\int_{V_f} |\nabla T|^2 dV_f}, \quad (3.9)$$

which has the same form as in single-phase flow except that the integral is extended only to V_f , the portion of the computational cell occupied by the fluid.

In order to establish a balance relation for the particle energy we take the scalar product of (2.11) with \mathbf{U}_p , of (2.12) with $\boldsymbol{\Omega}_p$ and add to find

$$\frac{d}{dt} \left(\frac{1}{2} m_p U_p^2 + \frac{1}{2} I_p \Omega_p^2 \right) - [\rho_p - \rho(T_p)] v_p \mathbf{g} \cdot \mathbf{U}_p = \mathbf{f}^{\text{hd}} \cdot \mathbf{U}_p + \mathbf{l}^{\text{hd}} \cdot \boldsymbol{\Omega}_p + \mathbf{f}^{\text{coll}} \cdot \mathbf{U}_p + \mathbf{l}^{\text{coll}} \cdot \boldsymbol{\Omega}_p. \quad (3.10)$$

Written in this form, the equation identifies the rate of change of the particle kinetic and gravitational potential energies. We define W_p^{hd} , the average work per unit time performed by the hydrodynamic forces and couples on the particles, and W_p^{coll} , the average work per unit time performed by the forces and couples arising from particle collisions, by

$$W_p^{\text{hd}} = \sum_{\alpha=1}^{N_p} \overline{(\mathbf{f}_{\alpha}^{\text{hd}} \cdot \mathbf{U}_{\alpha} + \mathbf{l}_{\alpha}^{\text{hd}} \cdot \boldsymbol{\Omega}_{\alpha})}, \quad W_p^{\text{coll}} = \sum_{\alpha=1}^{N_p} \overline{(\mathbf{f}_{\alpha}^{\text{coll}} \cdot \mathbf{U}_{\alpha} + \mathbf{l}_{\alpha}^{\text{coll}} \cdot \boldsymbol{\Omega}_{\alpha})}. \quad (3.11)$$

With these definitions, after taking a time average and recalling the definition (3.7) of E_p , (3.10) becomes

$$E_p = W_p^{\text{hd}} + W_p^{\text{coll}}, \quad (3.12)$$

stating that the average rate of change of the particle gravitational potential energy is balanced by the work per unit time performed by the flow and interparticle forces, as expected. The relation (3.12) affords us the possibility of an accuracy check on our simulations. The error, defined by

$$\text{error} = \frac{|E_p - (W_p^{\text{hd}} + W_p^{\text{coll}})|}{E_p}, \quad (3.13)$$

is shown in Tables III and V and is seen to be about 1.2% in one case and less than 1% in all the other ones.

It may also be noted that, with the previous definitions, (3.5) may be written

$$E_f = \Phi - W_p^{\text{coll}}, \quad (3.14)$$

with

$$\Phi = \frac{1}{2\mu_f} \overline{\int_{V_f} \boldsymbol{\tau} : \boldsymbol{\tau} dV_f}, \quad (3.15)$$

the average viscous energy dissipated by the fluid flow in the fluid volume per unit time. Equation (3.14) states that the average gravitational potential energy gained by the fluid per unit time, in the left-hand side, is dissipated by viscosity and by interparticle collision processes as could have been anticipated. In principle, the relation (3.14) could also provide an accuracy test for the simulations. However, obtaining Φ requires the calculation of the fluid velocity gradient in the geometrically very complex domain constituted by the computational domain with a spherical “hole” corresponding to each particle. Since one of the favorable features of the present numerical method is the relatively small number of cells per particle, the accurate calculation of this quantity presents a computational challenge that we did not think worth pursuing. (The calculation of the hydrodynamic force and couple on the particles does not require the explicit evaluation of $\boldsymbol{\tau}$.) Substituting the numbers presented below in Tables III and V into (3.14) one finds differences between 1% and 5% reaching, in one case, nearly 9%.

IV. NUMERICAL METHOD

The mathematical problem for the fluid is solved numerically by the PHYSALIS method, which has been thoroughly described in several earlier publications (see, e.g., Refs. [19,23]). The method relies on the use of analytic general solutions for momentum and energy to replace boundary conditions on the particle surfaces by equivalent conditions on the neighboring nodes of a regular Cartesian grid.

Consider for example the convection-diffusion energy equation in the neighborhood of a generic particle in the particle rest frame. Because of the no-slip condition at the particle surface, in this frame the fluid velocity is very small and convection can be neglected. Furthermore, it can be assumed that the fluid temperature at the grid nodes closest to the particle surface tracks the particle temperature with a negligible time lag. With these approximations, which are fully justified in Ref. [23], the convection-diffusion equation can be approximated locally by $\nabla^2 T = 0$. The most general solution of this equation around a spherical particle of radius a with a given temperature T_p , determined from (2.14), can be written as a series involving a superposition of spherical harmonics multiplied by known functions of the distance from the particle center,

$$T(\mathbf{x}, t) = T_p(t) + \sum_{\ell=0}^{\infty} \left[\left(\frac{r}{a} \right)^{\ell} - \left(\frac{a}{r} \right)^{\ell+1} \right] \sum_{m=-\ell}^{\ell} T_{\ell m}(t) Y_{\ell}^m(\theta, \phi). \quad (4.1)$$

Here ($r = |\mathbf{x}|$, θ , ϕ) are a system of spherical coordinates centered at the particle center. In particular, the first few coefficients $T_{\ell m}(t)$ are related to quantities appearing in (2.14) and (3.6) as the radial heat flux at the particle surface is given by

$$-\mathbf{q} \cdot \mathbf{n}_p = k_f [rT]_{r=a} = k_f \sum_{\ell=0}^{\infty} \frac{2\ell+1}{a} \sum_{m=-\ell}^{\ell} T_{\ell m} Y_{\ell}^m. \quad (4.2)$$

From the well-known orthogonality properties of the spherical harmonic functions we have

$$-\oint_{s_p} \mathbf{q} \cdot \mathbf{n}_p ds_p = 2\sqrt{\pi} a k_f T_{00}(t). \quad (4.3)$$

Similarly, we find

$$\oint_{s_p} (z - z_p) \mathbf{q} \cdot \mathbf{n}_p ds_p = -\sqrt{12\pi} a^2 k_f T_{10}. \quad (4.4)$$

If the coefficients $T_{\ell m}(t)$ are known, then a suitable truncation of the series can be used to assign the temperature on the grid nodes closest to the particle surface and this information can be used

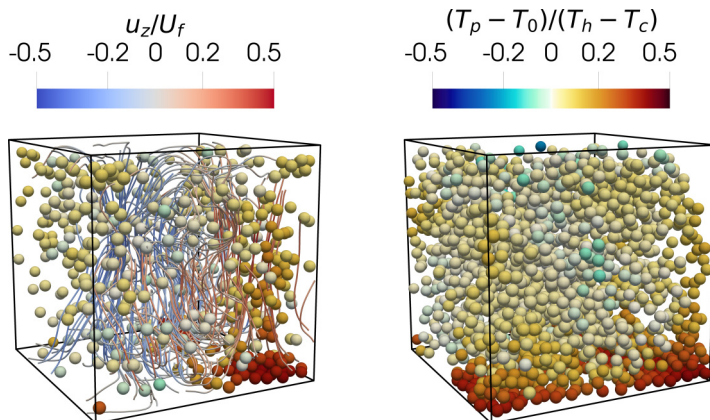


FIG. 1. Snapshots of simulations with 500 (left) and 2000 (right) particles with volume fractions 3.27% and 13.1%, respectively; for both the density ratio is $\rho_p/\rho_0 = 1.1$ and the ratio of specific heats $c_{pp}/c_{pf} = 1$. A few streamlines, colored according to the local vertical velocity, are drawn in the left figure but omitted for the right one as the large number of particles would block the view. The particles are colored according to their normalized temperature. The Rayleigh number is 10^7 and the Prandtl number is 1. Movies of these simulations are available as Supplemental Material [27].

to solve the (complete) convection-diffusion equation (2.4) throughout the fluid domain. Since the coefficients are unknown, the calculation proceeds by iteration, starting with guessed values. The procedure is similar for the momentum equation for which reliance can be made on a general solution of the momentum equation in the rest frame of each particle derived by Lamb (see, e.g., Ref. [24]). In this case, similarly to (4.3) and (4.4), the expansion coefficients provide directly the hydrodynamic force, couple, and higher-order multipoles. Particle-particle and particle-boundary collisions are handled by a soft-particle contact-force model summarized in Ref. [19]. The model, which provides the forces and the couples on the colliding particles, is based on work of Refs. [25] and [26] and the only adjustable parameter that it contains, other than the values determined by the previous investigators which we have left unchanged, is the dimensionless Young's modulus of the particle material defined by $Y = v_f^2 Y_d / [\rho_0 (1 - \sigma^2) g^2 d_p^4]$ with Y_d the dimensional modulus and σ Poisson's ratio. In the present calculation we take $Y = 10^6$.

Given the limited Reynolds number of the fluid-particle motion that we encounter in the present paper (see Table I), on the basis of earlier grid convergence studies, for the present simulations we have used uniform Cartesian grids with eight nodes per particle radius. Again on the basis of past experience, the summations in the general solution for the energy have been truncated to $\ell = 3$, i.e., to the first 16 terms. The same truncation has been used for all three families of coefficients necessary for the fluid momentum.

The use of periodicity conditions in the horizontal directions does not prevent the development of a horizontal drift of the particles and of the fluid bulk (the no-slip condition anchors in place the fluid layers near the horizontal boundaries). We have monitored this effect finding a slow drift with a mean velocity of a fraction of a percentage of the free-fall velocity. This artifact could be alleviated by a controller in the form of a small time-dependent horizontal pressure gradient but the drift was so small that such a measure did not seem necessary.

V. CUBIC CELL

Figure 1 shows snapshots from two simulations, one with 500 particles, on the left, the other with 2000 particles suspended in a Rayleigh-Bénard flow with $Ra = 10^7$ and $Pr = 1$ in a cell with aspect ratio 1. The particles are colored according to their normalized temperature

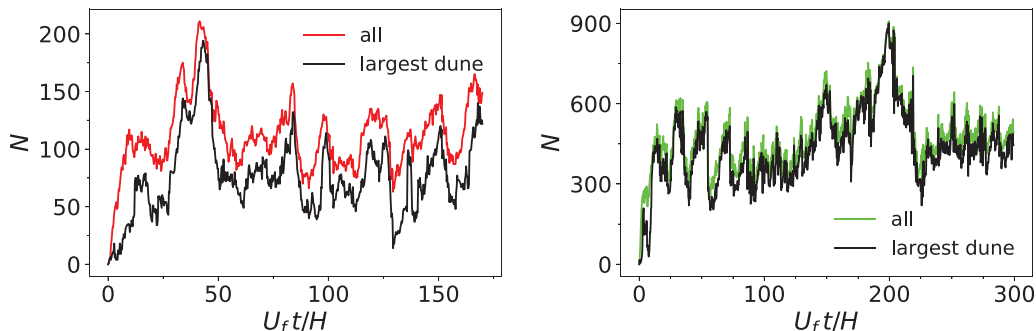


FIG. 2. The total number of bottom particles (in red in the left panel and in green in the right panel) and the number of particles in the largest bottom cluster (in black both panels); left and right panels for the simulations with 500 and 2000 particles, respectively.

$(T_p - T_0)/(T_h - T_c)$. The color on the streamlines in the left panel is according to the local fluid vertical velocity normalized by the free-fall velocity and gives an idea of the ascending and descending plumes in the cell. A better visualization is afforded by two movies available as Supplemental Material [27]. The length of each side of the cell is 20 particle diameters d_p so that, with $d_p = 2.5$ in dimensionless units, the range of all coordinates is $[-25, 25]$.

Periodicity and no-slip boundary conditions are applied on the vertical and horizontal faces of the cell, respectively. The time scale is $(d_p/2.5)^2/v_f$ and the velocity scale is $2.5 v_f/d_p$, in terms of which the free-fall velocity has the value $U_f = \sqrt{4000} \simeq 63.25$. The temperature at the cell base is fixed at $T_h = +2$ and at the cell top at $T_c = -2$, the thermal expansion coefficient is $\beta = 0.1$ and the gravity parameter $g = 200$. While in single-phase Rayleigh-Bénard convection the flow is entirely determined by the Rayleigh and Prandtl numbers and the cell aspect ratio, the addition of particles introduces several additional dimensionless groups which are connected to each other by the appearance of the same dimensional quantities in more than one of them. This circumstance renders necessary the specification of more quantities than would be necessary for single-phase flow. These additional dimensionless parameters characterizing the simulations are shown in Table I.

The simulation is started by arranging the particles randomly in the cell and freezing their position until they are released at the time $t = 0$ at which the fluid has reached a regime of statistically steady convection. Though fixed, the particles exchange heat with the fluid from the start of the simulation until the time $t = 0$ at which they are released.

In the course of the simulations there always is a significant number of particles on the bottom forming one or more heaps or clusters to which, following Ref. [16], we refer as “dunes.” The left panel of Fig. 2 shows a graph of the total number of bottom particles (in red) and of the number of particles in the largest bottom cluster (in black) for the simulation with 500 particles. The right panel is similar for $N_p = 2000$ with the total number of bottom particles in green and that of those in the largest dune in black. The fluctuations of the numbers show that the dunes are dynamic structures, although the number of particles associated with the largest dune closely tracks the total number of bottom particles signaling that the largest number of clustered particles always belong to a single dune. The mean number of suspended particles and related information is shown in Table II.

Clusters are identified by a variant of the “union-find” algorithm [28] which, given a set of points (in this case the position of the particle centers) identifies “islands,” or clusters of particles. In the present implementation a particle is declared to belong to a cluster when the distance of its surface from that of another particle in the cluster is less than ϵd_p , with ϵ a small parameter (unrelated to the particle collision model). A cluster containing at least one bottom particle, i.e., a particle the surface of which is closer to the cell bottom than ϵd_p , is declared a bottom cluster. All other particles, isolated or clustered, are declared suspended. An example of the clusters identified in this

TABLE II. Some results for the cubic domain: Total number of particles N_p , total volume fraction ϕ , number of suspended particles $N_{p,s}$, volume fraction of suspended particles ϕ_s , and Nusselt number Nu.

| N_p | ϕ | $N_{p,s}$ | ϕ_s | Nu |
|-------|--------|----------------|---------------------|------|
| 500 | 3.27% | 390 ± 18 | $(2.55 \pm 0.12)\%$ | 17.4 |
| 2000 | 13.1% | 1506 ± 100 | $(9.85 \pm 0.65)\%$ | 17.2 |
| 3000 | 19.6% | 1782 ± 180 | $(11.7 \pm 1.2)\%$ | 17.1 |

way is shown in Fig. 3 which is a snapshot from the simulation with 2000 particles. The centers of bottom or bottom-clustered particles are in black and centers of particles belonging to the same cluster are connected by red lines, while the centers of suspended particles are in blue. We have experimented with different values of ϵ , between 0.1 and 0.025, finding very small differences, comparable to the differences between the black and green lines in Fig. 2(b). A somewhat greater difference, comparable to that between the black and red lines of Fig. 2(a), is found by taking $\epsilon = 0$. In general, while the larger-scale trend of the curves does not change much, reducing ϵ has the effect of superimposing high-frequency fluctuations on the slower oscillations of the bottom-particles number. To avoid this fairly insignificant feature, the results shown here have been obtained with $\epsilon = 0.1$.

The dunes form because of the nature of the fluid flow near the cell bottom which is approximately horizontal and, by continuity, directed from regions under the descending plume to regions under the ascending one [29]. Bottom particles exposed to this flow are dragged toward the base of the ascending plume and gradually accumulate building up the dune. On the sides of the dune, the

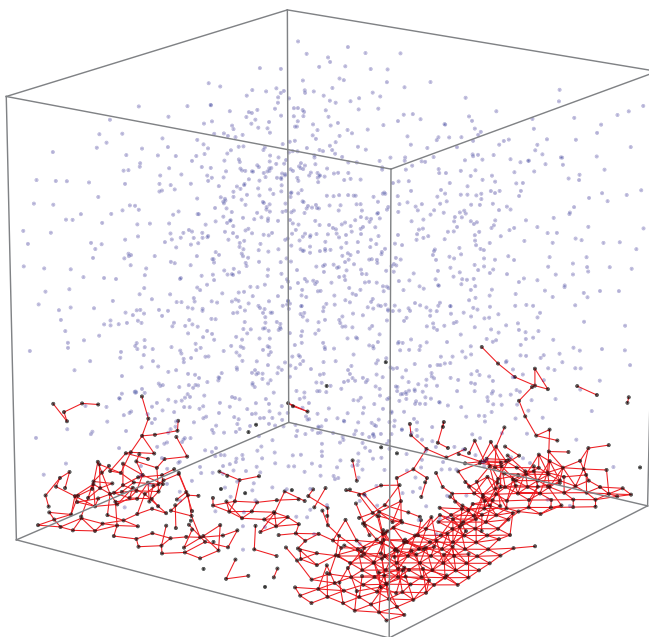


FIG. 3. Illustration of the performance of the union-find algorithm used to identify particles on the bottom or attached to particles on the bottom (black dots). The centers of particles belonging to the same cluster are connected by red lines. The centers of suspended particles are blue. One notices small clusters that appear attached to a vertical wall but, because of the use of periodicity conditions, are in fact attached to a bottom cluster cut through by the opposite wall.

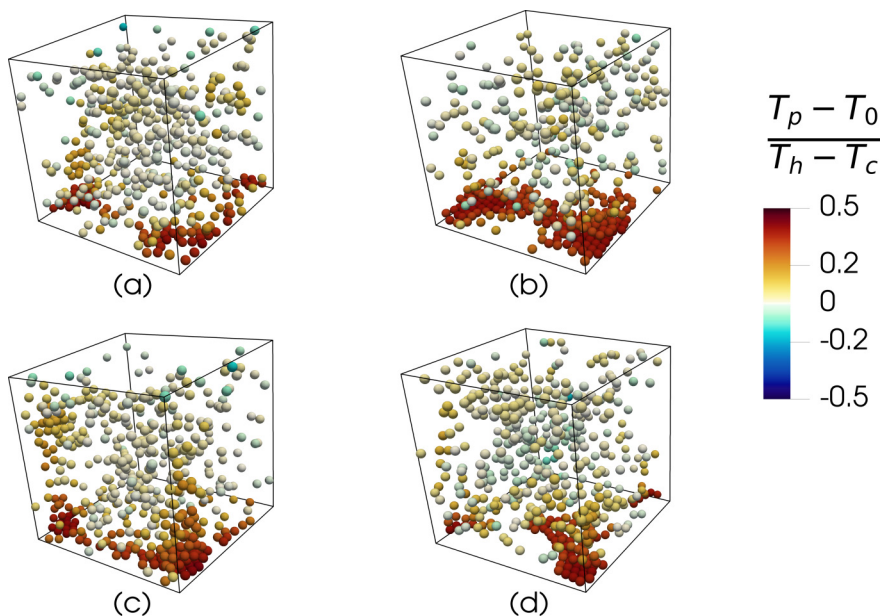


FIG. 4. Illustration of the phenomenon of dune buildup, eruption, and dissipation for particles with $c_{pp}/c_{pf} = 1$ for $N_p = 500$; see Fig. 2(a) for the number of particles in the dune at the times indicated. The incipient dune on the front left in (a) (time 27.9) accumulates an increasing number of particles [image (b), time 42.0] until the convection is so strong that the particles are lifted and the dune “erupts” [image (c), time 49.4], after which the dune is depleted [image (d), time 54.4] and particle accumulation begins anew.

velocity of the ascending fluid acquires a vertical component which is able to drag particles up the dune slope gradually building it up. At the same time, the heat flux at the cell bottom causes the temperature of the dune particles to increase, which strengthens the ascending plume. At some point, the plume becomes so strong that a large number of the dune particles is lifted and “erupts” from the top of the dune. The process goes on to repeat itself cyclically, although not periodically given the large number of degrees of freedom involved in the formation of the dune. This sequence of events, which is demonstrated in Fig. 4 and is clearly visible in the movie available in the Supplemental Material [27], explains the large oscillations of the number of dune particles visible in Fig. 2.

Figure 5 reveals some interesting changes occurring in the distribution of particles between bottom clusters and unattached particle clouds transported by convection as the particle number is increased. Figure 5(a) is the pdf of the time particles spend belonging to a bottom cluster (or directly on the cell bottom) while Fig. 5(b) is the pdf of the time particles spend suspended in the flow. The red, green, and black lines are for $N_p = 500$, 2000, and 3000, respectively. It can be seen in Fig. 5(a) that, as N_p increases, belonging to a cluster attached to the cell bottom becomes more probable although the attachment time decreases. Figure 5(b) shows that, for $N_p = 500$, the probability for a particle to be “in flight” has a single broad peak around $U_f \Delta t_s / H \sim 10$. The green line, for $N_p = 2000$ particles, exhibits two peaks, a broad one centered around $U_f \Delta t_s / H \sim 10$ and a sharper one centered around a considerably shorter duration $U_f \Delta t_s / H \sim 1$. The presence of two peaks signals the transition between two regimes, the second one of which becomes clear from the black line for $N_p = 3000$. It is seen here that the broader peak around $U_f \Delta t_s / H \sim 10$ has completely disappeared while the peak around $U_f \Delta t_s / H \sim 1$ has grown considerably in height and decreased in width. Furthermore, the probability of particles spending a sizable amount of time on the bottom, for example, $U_f \Delta t_b / H = 20$, is seen to decrease as N_p increases. Thus, for $N_p = 3000$, particles rapidly alternate between connection to, and disconnection from, bottom-connected groups. Since, as the

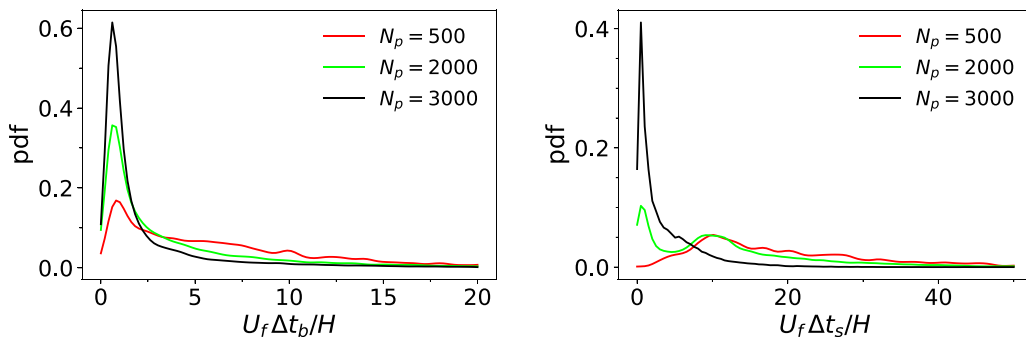


FIG. 5. (a) Probability density function of the time Δt_b particles spend belonging to a bottom cluster (or directly on the cell bottom). (b) Probability density function of the time Δt_s particles spend suspended in the flow. Red lines, $N_p = 500$; green lines, $N_p = 2000$; black lines $N_p = 3000$. For all these simulations $c_{pp}/c_{pf} = 1$.

particle volume fraction increases, eventually the system must become a porous medium, what we see here is the beginning of this transition, something akin to the first steps toward percolation.

The previous results are not significantly dependent on the particle specific heat, which was the same as that of the fluid for the simulations of Fig. 5. Figure 6 shows the pdf's of the time $N_p = 500$ particles spend in suspension and on the cell base for $c_{pp}/c_{pf} = 1$ and $c_{pp}/c_{pf} = 5$. The average time Δt_s spent in suspension does not depend significantly on the ratio of specific heats being $U_f \Delta t_s / H = 21.3$ and 21.9 , respectively, which implies that these flying particles are essentially passively carried by the flow without their different thermal interaction with the fluid being a significant factor in their behavior. This time is also considerably longer than the mean fluid circulation time $U_f t_c / H \sim 2$. Thus, even accounting for the fact that U_f represents an overestimation of the fluid velocity (see the color scale in Fig. 1 and Fig. 9), particles follow several fluid circulations before sedimenting. Their eventual falling to the cell bottom is a low-probability event consequence of the mildly chaotic nature of the present flow with $Ra = 10^7$ and of the relatively small difference between the particle and fluid densities.

The heat capacity is somewhat more consequential for the average time Δt_b particles spend on the cell bottom, either in isolation or in the dune, which is $U_f \Delta t_b / H = 7.26$ and 8.67 for the smaller and larger heat capacities, respectively. Larger-heat-capacity particles require a longer time to absorb heat, and it is only when they are hot enough that they can reinforce the plume sufficiently to lift them. Another interesting aspect of Fig. 6 is the difference between the long tail of the lifetime

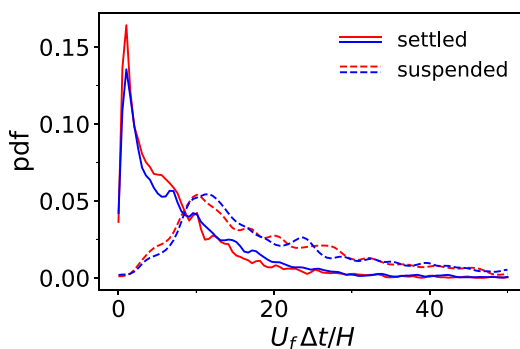


FIG. 6. Probability density function of the time particles spend on the cell bottom (solid) and suspended in the convective circulation (dashed) for $N_p = 500$, $c_{pp}/c_{pf} = 1$ (red), and $c_{pp}/c_{pf} = 5$ (blue).

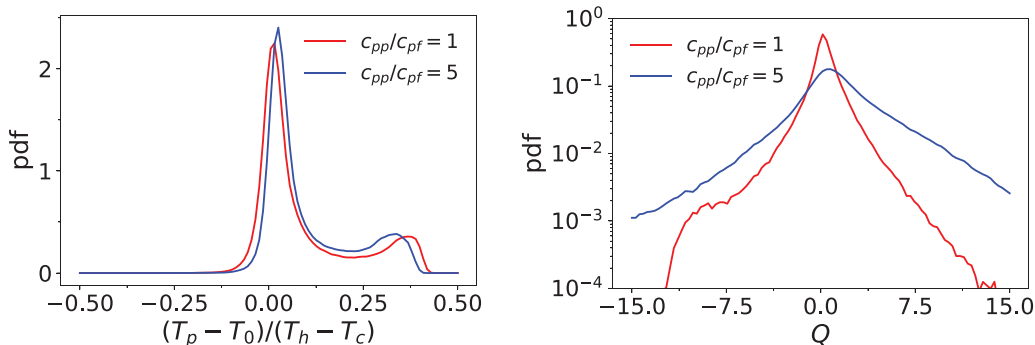


FIG. 7. (a) Probability density function for the particle temperature for different ratios of the particle-to-fluid specific heats. (b) Probability density function for the heat transferred to the fluid by the suspended particles; $Q > 0$, with Q defined in (2.14), indicates particles releasing heat to the fluid. The red lines are for $c_{pp}/c_{pf} = 1$ and the blue lines for $c_{pp}/c_{pf} = 5$ and $N_p = 500$.

pdf of the flying particles compared with the much shorter one of the bottom particles. It is evident that there is a vigorous resuspension mechanism at work which prevents particles to remain in a settled state too long. The time on the bottom is also shorter than the time between two successive “particle eruptions” from the dune which can be seen in Fig. 2(b). This implies that, between one eruption and the next, there is a large number of individual particle lift-up events for this rather small number of particles. The c_{pp}/c_{pf} -related differences that we have just described cannot be expected to have much influence in the transition with increasing N_p that we have seen in Fig. 5 because the long tail corresponding to settled particles tends to decrease with particle number.

Figure 7(a) is the probability density function of the particle temperature over the entire length of the simulations for $c_{pp}/c_{pf} = 1$ and $c_{pp}/c_{pf} = 5$ with $N_p = 500$. For both specific heats there are higher peaks slightly to the right of the reference temperature $T_0 = 0$, which is also close to the fluid temperature in the central region of the cell. These positive peaks are due to the fact that particles have a tendency to carry their thermal energy upward from the heated cell base. The higher- c_{pp} particles are slightly warmer than those with $c_{pp}/c_{pf} = 1$ because they are able to retain their temperature longer due to their higher thermal Stokes number (Table I). Both types of particles also exhibit a smaller and broader peak centered around $(T_p - T_0)/(T_h - T_c) \sim 0.3$ – 0.4 . This peak is produced by particles which are heated at the cell bottom. In this case it is the particles with $c_{pp}/c_{pf} = 1$ which are warmer, as their temperature rises more quickly than that of the higher- c_{pp} ones. Figure 7(b) is a similar probability density function for the energy exchange between the fluid and the suspended particles and positive when the particles heat the fluid. In keeping with the results in Fig. 7(a), for particles with $c_{pp}/c_{pf} = 5$ the maximum of the pdf corresponds to a slightly greater heat flow rate. A greater difference between the two results concerns the wings of the distributions. Particles with the smaller c_{pp} cool off quickly and their contribution to the larger positive values of Q is much smaller than that of the particles with $c_{pp}/c_{pf} = 5$. The difference is not as marked when the particles are heated by the fluid ($Q < 0$) and Q is moderate. However, the number of the smaller c_{pp} particles contributing to large negative values of Q is very small since these particles quickly adjust their temperature to that of the surrounding fluid, which reduces the temperature difference and, with it, the amount of heat transferred.

The joint pdf of the particle position and the heat transferred to the fluid [first term in the right-hand side of Eq. (3.8)] is shown in Fig. 8 for $c_{pp}/c_{pf} = 5$ (left) and 1. The heat transferred to the bottom particles [$Q < 0$, with Q defined in Eq. (2.14)] is greater the larger their heat capacity. As particles are transported upward the maximum of the pdf is slightly positive for the same reason as in Fig. 7(a). Particles with a larger heat capacity are able to maintain a temperature difference with

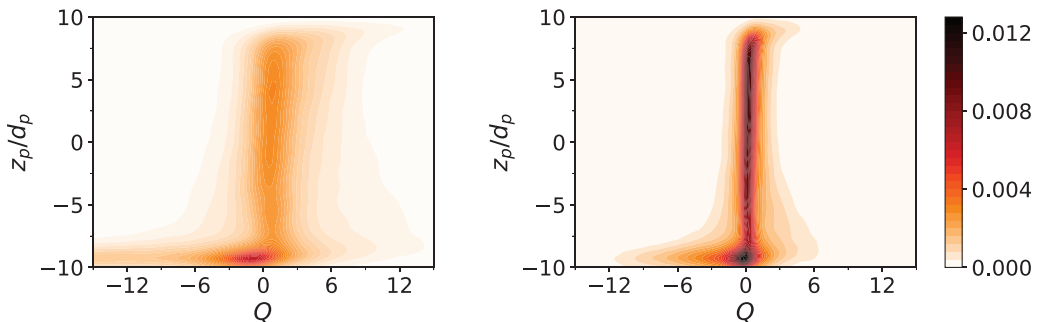


FIG. 8. Joint probability density function of the particle position, on the vertical axis, and of the heat they transfer to the fluid for $c_{pp}/c_{pf} = 5$ (left) and 1; Q is defined in (2.14).

the fluid for a longer time and, accordingly, their joint pdf is less peaked and more diffuse than for those with $c_{pp}/c_{pf} = 1$.

It is well known that the free-fall velocity (2.6) overestimates the magnitude of the actual velocity in the cell. This shortcoming has motivated the introduction of the “wind velocity,” which can be defined in different ways (see, e.g., Refs. [18,30,31]). Here we define it as the modulus of the mixture vertical velocity averaged over the midplane of the cell. This quantity is shown in Fig. 9 for the single-phase situation (dashed) and for increasing number of particles in the order red, green, and black. It is seen here that, for $N_p = 500$ (red line), the wind velocity is essentially the same as for the single-phase case (dashed), the only difference being a somewhat greater amplitude of the oscillations around a mean value of 0.12, nearly six times smaller than the free-fall velocity. With this result we can estimate the Reynolds number of the flow circulation in the cell as $Re \simeq 550$. The corresponding thickness δ of the viscous boundary layer on the cell base can then be estimated as $\delta = \sqrt{\nu_f H / U_{wind}} \simeq 2.1$, which is slightly smaller than the particle diameter d_p , $d_p/\delta = 1.2$. It can be deduced that the top of the particles is exposed to the circulating velocity of the fluid so that the particles can easily be pushed toward the base of the ascending plume. As the number of particles is increased to 2000 (green) and then to 3000 (black) the wind velocity progressively decreases as expected.

The running average of the present results for the bottom and top Nusselt numbers defined in (3.3) with $\rho_p/\rho_0 = 1.1$ and $c_{pp}/c_{pf} = 1$ is shown in Fig. 10(a) by the solid and dashed lines, respectively. The horizontal short-dashed line is the value of the single-phase Nusselt number computed for our situation, 16.9. With $Ra = 10^7$ and $Pr = 1$, the standard correlation $Nu = 0.069 Ra^{1/3} Pr^{0.074}$

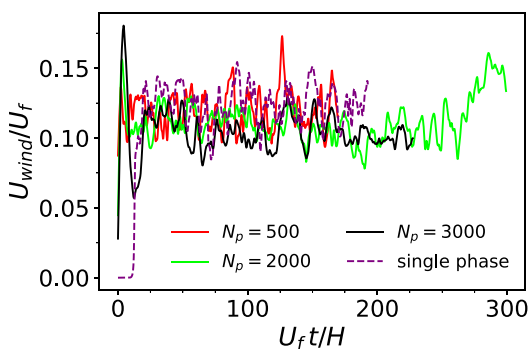


FIG. 9. Normalized wind velocity U_{wind}/U_f , defined as the cross-sectional average of the absolute value of the vertical mixture velocity at the cell midlevel, for the simulations in the cubic domain.

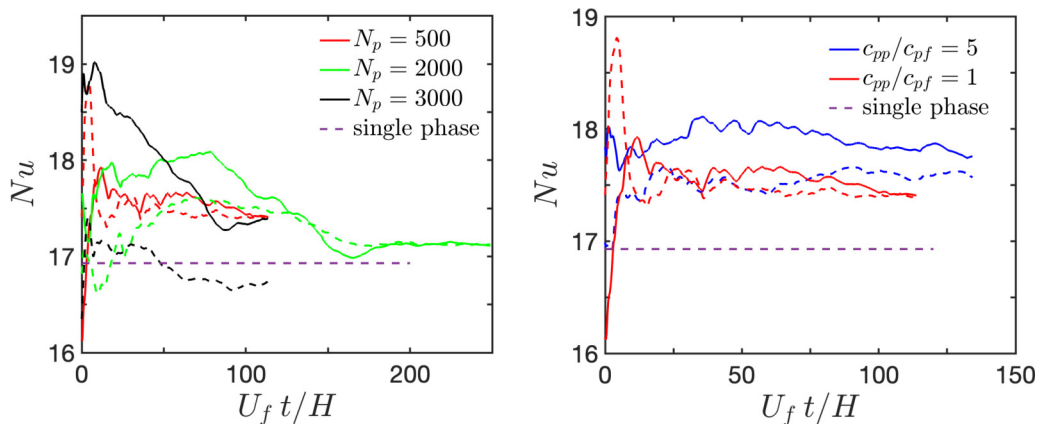


FIG. 10. (a) Running averages of the bottom (solid lines) and top (dashed lines) Nusselt numbers vs normalized time for the cubic domain with $c_{pp}/c_{pf} = 1$ in (a) and $c_{pp}/c_{pf} = 5$ in (b). In (a) the red lines are for $N_p = 500$, the green lines for $N_p = 2000$, and the black lines for $N_p = 3000$. For (b) $N_p = 500$. In both panels the horizontal dashed line is the computed single-phase value.

applicable to small aspect ratio (see, e.g., Ref. [32]) gives $Nu = 14.9$. The pairs of lines for $N_p = 500$ and 2000 converge quite well, but those for 3000 particles are still fairly distant from each other and it appears that substantially longer simulations would be needed for them to converge. While it is not possible to draw firm conclusions about the 3000-particle case, the results for $N_p = 500$ and 2000 are both slightly higher than the single-phase case in spite of the very close physical properties of the particles and the fluid. A likely explanation is that a particle maintains its integrity and is therefore able to carry its thermal energy all the way to the top of the cell while a fluid parcel tends to be deformed and broken up by the surrounding fluid in its ascent. This interpretation is strengthened by Fig. 10(b) in which the effect of the particle heat capacity on the Nusselt number is compared for $N_p = 500$. It is seen here that particles with a larger c_{pp} provide a modest increase in the total amount of heat transported through the cell. The small improvement of the Nusselt number seems rather fragile as the number of particles is increased since it is essentially gone for $N_p = 2000$. It appears that the increased load that the particles impose on the fluid circulation slows it down and ends up hurting the overall heat transport in spite of the greater effectiveness of the particles as heat carriers.

Particles gain gravitational potential energy by being suspended by the buoyancy-induced fluid flow. Following Ref. [17] one can define a conversion efficiency from fluid to particles gravitational energy by

$$\epsilon = \frac{E_p}{E_f}, \quad (5.1)$$

with E_f and E_p the rates of change of the gravitational potential energies of fluid and particles defined in (3.1) and (3.7), respectively. The results for E_f , E_p , and ϵ from the three-dimensional simulations described in this section are shown in Table III. The efficiency tracks fairly closely the particle volume fraction and is substantially greater than the estimate 0.6–0.9% given in Ref. [17] for reasons that will be discussed in Sec. VII. Table III also shows W_p^{hd} , the hydrodynamic work done by the fluid on the particles, and W_p^{coll} , the collision work, both defined in (3.11). It can be seen that all the particle quantities are approximately proportional to the number of particles, with those for $N_p = 2000$ and 3000 approximately four and six times those for $N_p = 500$, respectively. The fluid energy E_f decreases as N_p increases. Even with 3000 particles and a volume fraction of

TABLE III. Global averaged quantities characterizing the fluid and particle behavior as computed in the present simulations for the cubic domain. The fluid and particle potential energies E_f and E_p are defined in (3.1) and (3.7); Φ , defined in (3.15), is the energy dissipated by viscosity; W^{hd} , defined with W^{coll} in (3.11), is the hydrodynamic work rate of the fluid on the particles; W^{coll} is the rate of energy dissipation by particle-particle collisions; “error” is an estimate of the numerical error of the simulations defined in (3.13).

| N_p | ϕ | E_p | E_f | E_p/E_f | Φ | W_p^{hd} | W_p^{coll} | Error |
|-------|--------|---------------------|--------------------|-----------|--------------------|--------------------|----------------------|--------|
| 500 | 3.27% | 0.857×10^5 | 3.17×10^6 | 2.76% | 3.07×10^6 | 1.48×10^5 | -0.613×10^5 | 0.74% |
| 2000 | 13.1% | 3.04×10^5 | 2.85×10^6 | 10.7% | 2.51×10^6 | 5.66×10^5 | -2.62×10^5 | 0.018% |
| 3000 | 19.6% | 4.85×10^5 | 2.63×10^6 | 18.4% | 2.11×10^6 | 8.77×10^5 | -3.94×10^5 | 0.39% |

nearly 20%, the particle quantities are always about one order of magnitude smaller than the fluid energy E_f .

VI. QUASI-TWO-DIMENSIONAL CELL

Some aspects of the problem at hand can be investigated by means of less demanding computational simulations carried out in a smaller quasi-two-dimensional domain having the same height as the cubic domain of the previous section but with a footprint of dimensions $20d_p \times 3d_p$. We enlarge the long horizontal dimension to twice that used for the cubic domain in order to put into evidence two counter-rotating circulating streams with stagnation regions on the base and on the top of the domain (Fig. 11).

The importance of these streams in promoting the resuspension of the particles is illustrated by the snapshots shown in Fig. 11 in which the four panels are for $N_p = 150, 300, 500$, and 1000 particles (volume fraction $\phi = 3.27\%, 6.54\%, 10.9\%$, and 21.8% , respectively). The lines are instantaneous streamlines colored according to the vertical component of the fluid velocity. In all cases, around the small stagnation region where the countercirculating streams meet, a dune forms the size of which increases with the number of particles. The importance of this structure in promoting the resuspension of the particles is evident and will be further illustrated below.

The wind velocity for the quasi-two-dimensional simulations is shown in Fig. 12. The single-phase result is significantly greater than that for the cubic cell due to a more pronounced separation

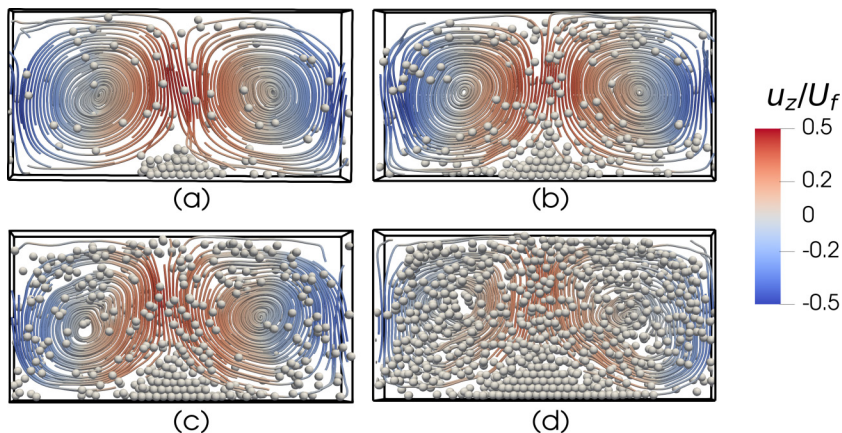


FIG. 11. Snapshots of flow in the quasi-two-dimensional cell with $N_p = 150$ particles in (a), $N_p = 300$ particles in (b), $N_p = 500$ particles in (c), and $N_p = 1000$ particles in (d). The streamlines are colored according to the value of the vertical fluid velocity.

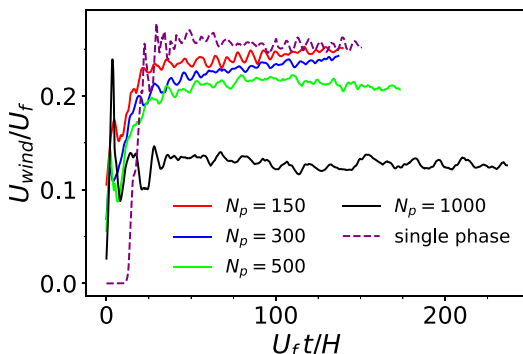


FIG. 12. Normalized wind velocity U_{wind}/U_f , defined as the cross-sectional average of the absolute value of the vertical mixture velocity at the cell midlevel, for the simulations in the quasi-two-dimensional domain.

between ascending and descending streams. As expected, the wind velocity decreases with increasing particle number. For the largest particle volume fraction, 21.8%, the slowing down is much stronger than the corresponding result for $\phi = 19.6\%$ for the cubic cell. A possible explanation is that, in the cubic cell, for large volume fractions the particles tend to form columnar structures which frequently form and breakup but are nevertheless effective in providing some form of support. As is made evident by Fig. 11, the situation is quite different in two dimensions as the particles can only be suspended when they are carried by the flow. Related information concerns the velocity distribution in the cell. Without particles the position of the ascending plume wanders and it is necessary to calculate the maximum upward flow velocity by calculating the maximum velocity at each instant and then averaging over time. By this procedure we find a value of 30.6 velocity units. With particles the maximum velocity is always above the dune which remains stable around the midpoint of the domain. We find 30.0 for 150 particles, 27.8 for 300, 25.0 for 500, and 18.6 for 1000.

Figure 13(a), showing the pdf of the time intervals during which particles remain suspended for $\rho_p/\rho_0 = 1.1$ and $c_{pp}/c_{pf} = 1$, is the analog, for the quasi-two-dimensional case, of Fig. 5(b) for the cubic domain, but it looks very much different as the series of peaks suggests harmonics of a process occurring on a fundamental timescale. A Fourier analysis of the data in Fig. 13(b), with the time dependence of the number of particles forming the dunes for $\rho_p/\rho_0 = 1.1$ and 1.2 and $N_p = 150$

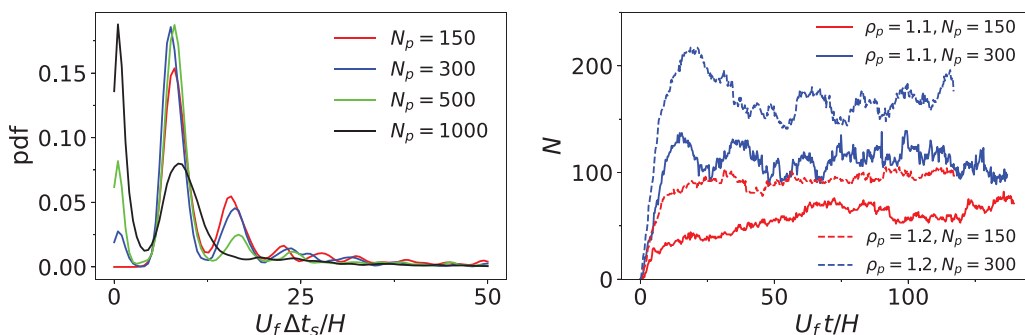


FIG. 13. (a) Probability density function for the dimensionless duration $U_f \Delta t_s/H$ of uninterrupted suspension for the quasi-two-dimensional simulations for $N_p = 150$ (red), 300 (blue), 500 (green), and 1000 (black). (b) Number of particles on the bottom of the computational domain vs time. Red lines are for $N_p = 150$ and blue lines for $N_p = 300$; solid lines are for $\rho_p/\rho_0 = 1.1$ and dashed lines for $\rho_p/\rho_0 = 1.2$; in all cases $c_{pp}/c_{pf} = 1$.

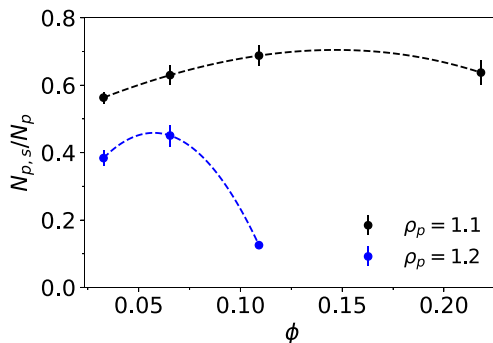


FIG. 14. Number of suspended particles $N_{p,s}$ normalized by the total number of particles N_p vs the volume fraction ϕ ; the vertical bars indicate the standard deviation. The dashed lines are cubic and quadratic interpolations for $\rho_p/\rho_0 = 1.1$ and 1.2 , respectively, to guide the eye.

and 300, is very noisy and hardly shows any distinctive peak. Analysis of the results demonstrates that the peak around $U_{ft}/H \sim 8$ in Fig. 13(a) corresponds to a mean circulation time of particles carried by the fluid stream. We can support this conclusion by assuming that the average trajectory is roughly circular with a diameter D so that the circulation time, normalized as in the horizontal scale of Fig. 13(a), is $(\pi D/U_{\text{wind}})U_{ft}/H$. With, from Fig. 12, $U_{\text{wind}} \simeq 15$, for this to equal $U_{ft}/H \sim 8$ it is necessary that $D \sim 30$ which is not an unreasonable estimate of an average trajectory circulating inside a square with side 50. The smaller peak around $U_{ft}/H \sim 16$ corresponds to particles which are carried around twice before falling to the bottom of the cell, and so on. An observation that supports this interpretation is that the position of the peaks shifts slightly to the right as the number of particles increases due to the decrease of the circulation velocity that can be seen in Fig. 12. These results illustrate a fundamental difference between the three-dimensional simulations and the quasi-two-dimensional ones which can be traced back to the much greater number of degrees of freedom of dune shape and size in the larger simulations. Nevertheless, in spite of their limitations, the two-dimensional simulations are instrumental in understanding and proving the essential importance of dunes for particle resuspension as we further illustrate below. Another feature worth noting in Fig. 13(a) is that, while the height of the peak around $U_{ft}/H = 8$ does not differ very much among the results for $N_p = 150, 300$, and 500 , it becomes much smaller for $N_p = 1000$, indicating a much less orderly particle circulation. A similar strong effect of particle number increase from 500 to 1000 can be seen on the wind velocity in Fig. 12.

The average number of suspended particles $N_{p,s}$ normalized by N_p is shown vs the volume fraction ϕ in graphical form in Fig. 14 for $\rho_p/\rho_0 = 1.1$ and 1.2 ; the lines are interpolating polynomials intended mostly as a guide to the eye. The same information is presented in tabular form in Table IV. In all cases the data suggest the presence of a maximum which is reached at a

TABLE IV. Quasi-two-dimensional simulations: Total number of particles N_p , total volume fraction ϕ , number of suspended particles $N_{p,s}$, volume fraction of suspended particles ϕ_s , and Nusselt number Nu.

| N_p | ϕ | $N_{p,s}$ | ϕ_s | Nu |
|-------|--------|--------------|---------------------|------|
| 150 | 3.27% | 84 ± 2 | $(1.84 \pm 0.05)\%$ | 16.5 |
| 300 | 6.54% | 189 ± 9 | $(4.12 \pm 0.19)\%$ | 16.4 |
| 500 | 10.9% | 344 ± 15 | $(7.50 \pm 0.34)\%$ | 16.3 |
| 1000 | 21.8% | 638 ± 40 | $(13.9 \pm 0.87)\%$ | 15.2 |

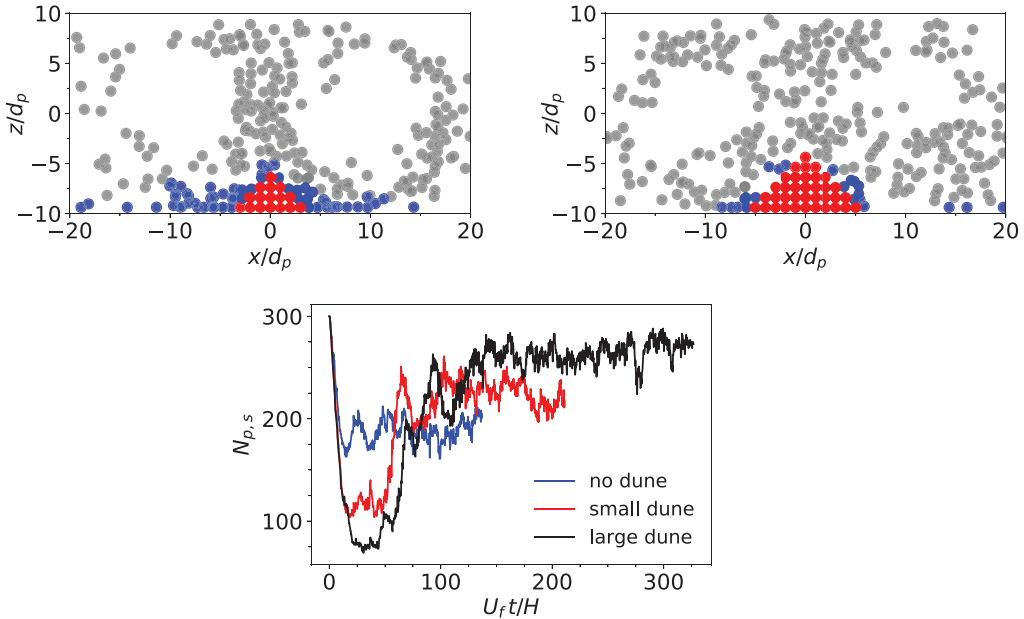


FIG. 15. Snapshots of the performance of artificial dunes (in red) for particle suspension. As can be seen in (c), which shows the number of suspended particles as a function of time, the smaller dune [in (a)] is less effective than the larger one [in (b)] in causing particle resuspension. In both cases the number of mobile particles is 300, their density $\rho_p/\rho_0 = 1.1$, and $c_{pp}/c_{pf} = 1$.

significantly smaller volume fraction for $\rho_p/\rho_0 = 1.2$ than 1.1. As long as N_p is not too large, the number of suspended particles increases more than proportionally to the total number of particles. The mechanism responsible for this behavior is the increase of the dune size with particle number as larger dunes are better “launching pads” for particle suspension.

To support this statement we carried out simulations with small and large artificial dunes constructed with particles held fixed (in red) as in Figs. 15(a) and 15(b). The particles on the ground or connected to particles on the ground (in the manner described in the previous section) are blue and suspended particles are gray. In both these examples the total number of free particles is the same, $N_p = 300$, but it can be seen that the number of particles suspended by the larger dune (right panel) is greater than that suspended by the smaller dune, and that the “queue” of particles “waiting” to be suspended is significantly longer for the small dune. The number of suspended particles is shown as a function of time in Fig. 15(c) starting from the instant $t = 0$ at which the particles are released. In the dune-free cell the circulation is fully developed at $t = 0$ and therefore, while some particles initially slump, they recover fairly quickly. Dunes, however, take a longer time to warm up and, accordingly, the circulation in the cell takes a longer time to develop. With little upward flow to suspend them, when the particles are released they slump to a lower value than in the dune-free case. Later, however, the ordering is reversed with the larger dune able to suspend the largest number of particles. Another interesting and related observation is that the ascending plume is thinner for the smaller dune so that particles have to crowd into it to get suspended.

Figure 16 shows running averages of the bottom (solid lines) and top (dashed lines) Nusselt numbers for the four particle numbers of these simulations. The bottom and top lines show an acceptable degree of convergence as the simulation time increases except for $N_p = 1000$ for which they are still quite distant from each other. As in the three-dimensional case, we find a modest improvement in the heat transfer for $N_p = 150$, which quickly deteriorates as N_p is increased. Although not converged, the results for $N_p = 1000$ suggest a significant decrease of the Nusselt

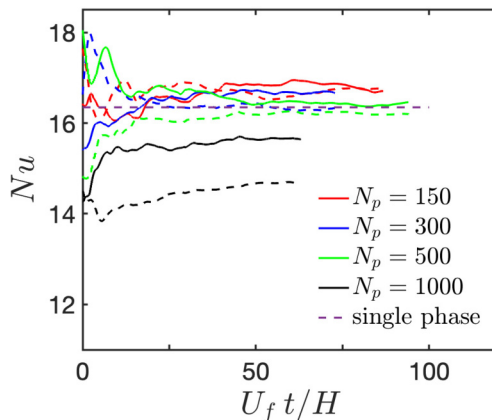


FIG. 16. Running averages of the bottom (solid lines) and top (dashed lines) Nusselt numbers vs normalized time for the quasi-two-dimensional simulations; $N_p = 150$ (red), $N_p = 300$ (blue), $N_p = 500$ (green), and $N_p = 1000$ (black). The dashed horizontal line is the computed single-phase value.

number for this case likely due to the slowing circulation velocity caused by the increased viscous dissipation and mixture weight.

Table V shows for the quasi-two-dimensional simulations the same calculated parameters shown in Table III for the three-dimensional case. The volume of the cubic cell is about 3.33 times as large as that of the other one. For the smallest volume fraction, about 3.27% for both, the ratio of the corresponding fluid energies E_f is quite close to this ratio indicating a similar energy density but, for the largest volume fraction, around 20%, the energy of the two-dimensional cell is about 4 times smaller than that of the cubic cell implying a stronger sensitivity to specifics of the geometry. Due to the smaller energy, all the particle quantities of the two-dimensional cell are smaller than those of the cubic cell, but the conversion efficiency of potential energy from fluid to particles is about the same.

VII. CONCLUSIONS

In the present paper we have demonstrated by means of particle-resolved numerical simulations the key role played by bottom-forming dunes in particle resuspension in Rayleigh-Bénard convecting systems with a Rayleigh number of 10^7 and a unity Prandtl number. Our results confirm the experimental observations reported in Ref. [16], where the dune-suspension mechanism was first discovered, seemingly without much further consideration in the literature. The simulations were conducted in two cells, one a cube with aspect ratio 1, the other a quasi-two-dimensional cell with the same height and aspect ratio 2, but a thickness (in the horizontal

TABLE V. Global averaged quantities characterizing the fluid and particle behavior as computed in the present simulations for the quasi-two-dimensional domain. See the caption to Table III for a definition of the quantities shown.

| N_p | ϕ | E_p | E_f | E_p/E_f | Φ | W_p^{hd} | W_p^{coll} | Error |
|-------|--------|--------------------|--------------------|-----------|--------------------|--------------------|---------------------|-------|
| 150 | 3.27% | 1.45×10^4 | 9.00×10^5 | 1.61% | 8.68×10^5 | 3.71×10^4 | -2.25×10^4 | 1.24% |
| 300 | 6.54% | 4.85×10^4 | 8.68×10^5 | 5.59% | 7.78×10^5 | 11.5×10^4 | -6.56×10^4 | 0.82% |
| 500 | 10.9% | 7.78×10^4 | 8.28×10^5 | 9.40% | 7.06×10^5 | 16.2×10^4 | -8.32×10^4 | 0.79% |
| 1000 | 21.8% | 12.1×10^4 | 6.94×10^5 | 17.4% | 5.29×10^5 | 22.4×10^4 | -10.4×10^4 | 0.15% |

direction) of only three particle diameters. In both cases the maximum particle volume fraction was around 20%.

Dunes form because the fluid flow near the cell bottom is nearly horizontal and directed from the base of the descending plumes toward that of the rising ones. Particles captured in this flow therefore collect around the base of the ascending plumes, form a dune and are pushed toward the top of it thereby acquiring a vertical velocity component which facilitates their entrainment into the rising fluid. It is evident from this description that dune formation will be prevalent when the particle diameter d_p is not too small compared with the thickness δ of the viscous boundary layer as in our paper, in which $d_p/\delta \simeq 1$. When $d_p \ll \delta$ one may expect that suspension would be caused mainly by large velocity fluctuations in the flow associated with turbulent bursts (see, e.g., Ref. [33]). This process is distinct from particle transport along the bottom, which occurs also in laminar flow (see, e.g., Ref. [34]), although both processes are often parametrized in terms of the Shields number $\tau_w/[(\rho_p - \rho)gd_p]$, with τ_w the bottom stress. Viscous bottom transport underlies the interpretation of Solomatov and Stevenson (1993) who based their study on an analogy of the particulate system with a system consisting of two superposed layers of miscible fluids with different densities [35]. This analogy led them to estimate the efficiency of conversion of the fluid energy into particulate potential energy to be 0.6–0.9%, far smaller than our results in which the calculated efficiency can approach 20%. When the particles are not too deeply immersed in the viscous boundary layer at the cell bottom, therefore, resuspension by dunes appears to be much more efficient than resuspension by shear. As a point of interest it may be mentioned that dune formation is also observed in sediment transport in laminar flow, where they seem to be only a consequence of the destabilization of the initial flat bed and are not observed to lead to particle suspension [36].

We have found that larger dunes are more effective than smaller ones in causing resuspension and that, up to a point, dune size increases with particle number and weight in both three and quasi two dimensions. Dunes are not static structures: The number of particles forming them depends on time, much more strongly in three than in two dimensions. In fact, in three dimensions one observes what may be called “breathing” of dunes, recurring episodes in which nearly half of the dune-forming particles are erupted upward over a short period of time [Fig. 2(b)]. The dune then builds up again over times of the order of tens of cell circulation times, erupts and so forth in a repeatable, although not periodic, series of similar events. In two dimensions the variability is much more limited [Fig. 13(b)] and the particles follow in a more predictable fashion the fluid circulation going around the loop one, two or more times before falling to the ground and then being resuspended. The fluid energy density is comparable in the two cells that we have studied but, since the cubic cell has a volume about three times as large as the other one, the energy content of the latter is smaller and, correspondingly, all the particle quantities (energy, hydrodynamic work, collision work) are also smaller. On the other hand, the energy conversion efficiency from fluid to particles at a comparable volume fraction is quite similar between the two cases.

For the largest volume fraction (about 20%) there were clear indications from the three-dimensional simulation of an approach toward a porous-medium behavior with a very frequent formation and disintegration of long particle chains. In two dimensions, instead, the particles formed a long-lived layer on the cell bottom which occasionally was seen to break up leading to particle resuspension. In both cells a small amount of light particles (up to a few percentages, with $\rho_p/\rho_0 = 1.1$) has a beneficial effect on the Nusselt number, but larger volume fractions slow down the circulation by increasing the mean mixture density and end up decreasing the Nusselt number.

The addition of particles greatly increases the number of dimensionless parameters necessary to characterize the flow. Together with the duration of typical simulations (from a few weeks to two months and more) this feature has limited our exploration of parameter space and has confined us to a relatively small Rayleigh number, 10^7 . It would be very interesting to increase this value, explore the effect of the fluid Prandtl number, increase and decrease the particle diameter, study the effect of the particle thermal properties, investigate the role played by their mechanical and thermal Stokes numbers, and so forth. The availability of particle-resolved numerical methods renders now

possible the study of physical aspects of particulate Rayleigh-Bénard convection which could not be investigated on the basis of point-particle models.

ACKNOWLEDGMENTS

The authors are grateful to Dr. Daniel Floryan (University of Houston) and Dr. Rodolfo Ostilla Monico (Universidad de Cádiz, Spain) for useful comments and suggestions. The authors acknowledge the use of the Carya and Sabine clusters and are grateful to Dr. J. Ebalunode of the UH Research Computing Data Core for his support. This study has been supported in part by the U.S. National Science Foundation CBET TTP under Grant No. 2053204.

-
- [1] A. F. Stein, R. R. Draxler, G. D. Rolph, B. J. B. Stunder, M. D. Cohen, and F. Ngan, NOAA's HYSPLIT atmospheric and dispersion modeling system, *Bull. Am. Meteorol. Soc.* **96**, 2059 (2015).
 - [2] H. S. Auta, C. U. Emenike, and S. H. Fauziah, Distribution and importance of microplastics in the marine environment: A review of the sources, fate, effects, and potential solutions, *Environ. Int.* **102**, 165 (2017).
 - [3] L. Elkins-Tanton, Magma oceans in the inner solar system, *Annu. Rev. Earth Planet. Sci.* **40**, 113 (2012).
 - [4] A. Xu, S. Tao, L. Shi, and H.-D. Xi, Transport and deposition of dilute microparticles in turbulent thermal convection, *Phys. Fluids* **32**, 083301 (2020).
 - [5] S. Balachandar, S. Zaleski, A. Soldati, G. Ahmadi, and L. Bourouiba, Host-to-host airborne transmission as a multiphase flow problem for science-based social distance guidelines, *Int. J. Multiphase Flow* **132**, 103439 (2020).
 - [6] S. Rayegan, C. Shu, J. Berquist, J. Jeon, L. Zhou, L. Z. Wang, H. Mbareche, P. Tardif, and H. Ge, A review on indoor airborne transmission of COVID-19 modelling and mitigation approaches, *J. Build. Eng.* **64**, 105599 (2023).
 - [7] V. Patočka, E. Calzavarini, and N. Tosi, Settling of inertial particles in turbulent Rayleigh-Bénard convection, *Phys. Rev. Fluids* **5**, 114304 (2020).
 - [8] P. Oresta and A. Prosperetti, Effects of particle settling on Rayleigh-Bénard convection, *Phys. Rev. E* **87**, 063014 (2013).
 - [9] P. Oresta, F. Fornarelli, and A. Prosperetti, Multiphase Rayleigh-Bénard convection, *Mech. Eng. Rev.* **1**, FE0003 (2014).
 - [10] H. J. Park, K. O'Keefe, and D. H. Richter, Rayleigh-bénard turbulence modified by two-way coupled inertial, nonisothermal particles, *Phys. Rev. Fluids* **3**, 034307 (2018).
 - [11] R. Puragliesi, A. Dehbi, E. Leriche, A. Soldati, and M. O. Deville, DNS of buoyancy-driven flows and Lagrangian particle tracking in a square cavity at high Rayleigh numbers, *Int. J. Heat Fluid Flow* **32**, 915 (2011).
 - [12] B. Gereltbyamba and C. Lee, Behavior of settling inertial particles in a differentially heated cubic cavity at moderate Rayleigh number, *J. Mech. Sci. Technol.* **32**, 3169 (2018).
 - [13] S. Takeuchi, T. Tsutsumi, K. Kondo, T. Harada, and T. Kajishima, Heat transfer in natural convection with finite-sized particles considering thermal conductance due to inter-particle contacts, *Comput. Therm. Sci.* **7**, 385 (2015).
 - [14] J. C. Gu, S. Takeuchi, and T. Kajishima, Influence of Rayleigh number and solid volume fraction in particle-dispersed natural convection, *Int. J. Heat Mass Transfer* **120**, 250 (2018).
 - [15] S. Takeuchi, Y. Miyamori, J. C. Gu, and T. Kajishima, Flow reversals in particle-dispersed natural convection in a two-dimensional enclosed square domain, *Phys. Rev. Fluids* **4**, 084304 (2019).
 - [16] V. Solomatov, P. Olson, and D. Stevenson, Entrainment from a bed of particles by thermal convection, *Earth Planet. Sci. Lett.* **120**, 387 (1993).
 - [17] V. S. Solomatov and D. J. Stevenson, Suspension in convective layers and style of differentiation of a terrestrial magma ocean, *J. Geophys. Res.: Planets* **98**, 5375 (1993).

- [18] G. Ahlers, S. Grossmann, and D. Lohse, Heat transfer and large scale dynamics in turbulent Rayleigh-Bénard convection, *Rev. Mod. Phys.* **81**, 503 (2009).
- [19] A. Sierakowski and A. Prosperetti, Resolved-particle simulation by the Physalis method: Enhancements and new capabilities, *J. Comput. Phys.* **309**, 164 (2016).
- [20] R. Clift, J. Grace, and M. Weber, *Bubbles, Drops, and Particles* (Academic Press, NY, 1978).
- [21] W. E. Ranz and W. R. Marshall, Evaporation from drops, *Chem. Eng. Prog.* **48**(3), 141 (1952).
- [22] T. L. Bergman, A. Lavine, F. P. Incropera, and D. P. DeWitt, *Fundamentals of Heat and Mass Transfer*, 8th ed. (Wiley, Hoboken NJ, 2018).
- [23] Y. Wang, A. Sierakowski, and A. Prosperetti, Fully-resolved simulation of particulate flows with particles-fluid heat transfer, *J. Comput. Phys.* **350**, 638 (2017).
- [24] S. Kim and S. J. Karrila, *Microhydrodynamics: Principles and Selected Applications* (Butterworth-Heinemann, Boston, MA, 1991).
- [25] Y. Tsuji, T. Tanaka, and T. Ishida, Lagrangian numerical simulation of plug flow of cohesionless particles in a horizontal pipe, *Powder Technol.* **71**, 239 (1992).
- [26] G. Barnocky and R. H. Davis, Elastohydrodynamic collision and rebound of spheres: Experimental verification, *Phys. Fluids* **31**, 1324 (1988).
- [27] See Supplemental Material at <http://link.aps.org/supplemental/10.1103/PhysRevFluids.9.054301> for movies of 2000 particles in the three-dimensional cell and 500 particles in the quasi-two-dimensional cell.
- [28] B. A. Galler and M. J. Fisher, An improved equivalence algorithm, *Commun. ACM* **7**, 301 (1964).
- [29] X. Chen, R. Ostilla Monico, D. Floryan, and A. Prosperetti, Particle resuspension in two-phase dispersed Rayleigh-Bénard convection (unpublished).
- [30] B. Castaing, G. Gunaratne, F. Heslot, L. Kadanoff, A. Libchaber, S. Thomae, X.-Z. Wu, S. Zaleski, and G. Zanetti, Scaling of hard thermal turbulence in Rayleigh-Bénard convection, *J. Fluid Mech.* **204**, 1 (1989).
- [31] L. P. Kadanoff, Turbulent heat flow: Structures and scaling, *Phys. Today* **54**(8), 34 (2001).
- [32] A. Bejan, *Convection Heat Transfer*, 4th ed. (Wiley, New York, 2013).
- [33] Y. Niño, F. Lopez, and M. Garcia, Threshold for particle entrainment into suspension, *Sedimentology* **50**, 247 (2003).
- [34] M. Ouriemi, P. Aussillous, M. Medale, Y. Peysson, and E. Guazzelli, Determination of the critical Shields number for particle erosion in laminar flow, *Phys. Fluids* **19**, 061706 (2007).
- [35] P. Olson, An experimental approach to thermal convection in a two-layered mantle, *J. Geophys. Res.* **89**, 11293 (1984).
- [36] M. Ouriemi, P. Aussillous, and E. Guazzelli, Sediment dynamics. Part 2. Dune formation in pipe flow, *J. Fluid Mech.* **636**, 321 (2009).